PERGAMON

International Journal of Solids and Structures 38 (2001) 5081–5095

INTERNATIONAL JOURNAL OF SOLIDS and STRUCTURES

www.elsevier.com/locate/ijsolstr

Modelling of localisation and scale effect in thick-walled cylinders with gradient elastoplasticity

A. Zervos [a,b,*], P. Papanastasiou [b], I. Vardoulakis [a]

[a] *Section of Mechanics, National Technical University of Athens, 5 Heroes of Polytechnion Avenue, Zografou 157 73, Greece*
[b] *Schlumberger Cambridge Research, High Cross, Madingley Road, Cambridge CB3 0EL, UK*

Received 25 May 2000

Abstract

We model the progressive localisation of deformation which causes failure around thick-walled cylinders under external radial pressure. The study is based on a second-gradient elastoplastic model developed to regularise the ill-posedness caused by material strain-softening behaviour. The stress increment is related to both the strain increment and its Laplacian. The gradient terms introduce an internal length scale to the material allowing robust modelling of its post-peak behaviour. The numerical implementation is based on a C^1 finite element displacement formulation. Mesh insensitivity in terms of load–displacement and failure mechanism is demonstrated. The internal length in the constitutive equations enables modelling of the scale effect in thick-walled cylinders, according to which the load required to induce failure appears to be much larger for small holes than for large holes.

Keywords: Gradient elastoplasticity; Gradient plasticity; Thick-walled cylinder; Localisation of deformation; Shear band; Scale effect

1. Introduction

Failure in solids and structures is often characterised by localisation of deformation in narrow zones of intense shearing in the form of shear bands or shear interface layers. In advanced loading states the material in these bands undergoes significant deformation and degradation of its mechanical properties, while the rest of the material remains rather inert. Evidence from triaxial, biaxial and ring simple shear experiments on geomaterials suggests that the localisation bands have a finite thickness (Mühlhaus and Vardoulakis, 1987).

Another characteristic of geomaterials is the dependence of their mechanical behaviour, stiffness and strength, on the dimensions of the tested specimens. This dependence of the strength on the geometrical

* Corresponding author. Address: Schlumberger Cambridge Research, High Cross, Madingley Road, Cambridge CB3 0EL, UK. Tel.: +44-1223-325-201; fax: +44-1223-327-019.
E-mail address: a.zervos@mechan.ntua.gr (A. Zervos).

0020-7683/01/$ - see front matter
PII: S0020-7683(00)00337-1

dimensions of a structure is called *scale effect*. In the structures community, the most well known example of scale effect is the dependence of the tensile strength and fracture toughness of concrete and other heterogeneous materials, as measured in tensile tests, on the specimen dimensions (Mihashi et al., 1994; van Vliet, 2000). A less well known problem of scale effect is the dependence of the hollow cylinder strength on the hole size. The hollow cylinder test is the standard laboratory test used in petroleum, geotechnical and mining engineering for assessing the stability of underground openings such as cavities and wellbores. Tests performed on hollow cylinders with holes of different sizes showed that the load required to induce failure appears to be much higher for small holes than for large holes (Papamichos and van den Hoek, 1995). Cylinders of small internal diameter consistently break under higher external pressure than cylinders of bigger internal diameter, resulting in failure pressures that may differ as much as 300%. Indeed, the most dominant factor of strength in the range of wellbore perforation size (diameter less than 25 mm) is the scale effect. Because of this strong scale effect, proper interpretation of experimental data, which are usually obtained from small size holes, and correct extrapolation to field dimensions are open issues. We remark that classical stress analysis (e.g. elastoplasticity) is unable to model the scale effect since the governing equations can be written in a dimensionless form, predicting for all the geometrically similar cylinders the same failure pressure. Therefore, in order to assess the ultimate stability of a hollow cylinder, a model must (a) be based on localisation of deformation as the most robust failure criterion and (b) be capable to address the scale effect.

Modelling of progressive localisation of deformation requires material softening to be included in the constitutive equations i.e. the material is considered to lose strength with straining. However, this leads to computational problems as the governing equations become ill-posed (Vardoulakis and Sulem, 1995). The shear band thickness remains indeterminate and numerical computations in the post-bifurcation regime are pathologically mesh dependent. Ill-posedness of the governing equations can be remedied by resorting to higher order continuum theories. These theories take into account the material microstructure by introducing an extra parameter of *material length*. This parameter can be typically related to the mean grain size, the microcrack length or some other characteristic length scale of the material. Higher order theories presented in the literature are the Cosserat continuum theory (Mühlhaus and Vardoulakis, 1987; Papanastasiou and Vardoulakis, 1992), the Mindlin theory (Mindlin, 1964), the non-local continuum (Pijaudier-Cabot and Bažant, 1987; Tvergaard and Needleman, 1995), gradient plasticity (Aifantis, 1984a,b, 1987; Vardoulakis and Aifantis, 1991; Vardoulakis et al., 1992; Vardoulakis and Frantziskonis, 1992; Fleck and Hutchinson, 1993; Pamin, 1994; Ramaswamy and Aravas, 1998a,b) and, recently, gradient elastoplasticity (Zervos et al., 2001). With higher-order theories the shear band thickness is no longer indeterminate since it scales with the material length. This allows mesh-independent post-peak localisation computations, which are able to capture the localised patterns. In addition, since the existence of the material length allows for differentiating between "small" and "large" geometries, scale effect arises naturally in the material behaviour.

Other related work is the studies of bifurcation problems for the borehole and hollow cylinder test based on classical plasticity and conventional perturbation methods for a rigid-plastic (Vardoulakis and Papanastasiou, 1988) and elastoplastic (Papanastasiou and Durban, 1999) material. The solution of the problem consisted in determining the lowest load which could cause warping at the surface of the hole. Mathematically, bifurcation was possible for a threshold load at which the incremental equations of equilibrium admit a non-unique solution. It was found that the most critical deformation mode of sinusoidal form is the one of infinite wave number which corresponds to surface instabilities. Perturbation methods in conjunction with higher order theories were used in the case of a Cosserat continuum by Papanastasiou and Vardoulakis (1989), and in the case of gradient plasticity by Vardoulakis et al. (1994). The existence of material length in these theories leads to *wave number selection*, yielding a finite wave number for the critical instability. Nevertheless, the perturbation approach predicts a lower bound of loading level at which localisation may initiate, without providing any information on how the localised pattern resulting in failure

might evolve. A closer related study can be found in Papanastasiou and Vardoulakis (1992), where post-bifurcation analysis with a Cosserat finite element model was carried out for modelling the progressive localisation and scale effect. More recently, strain gradient plasticity was used by Shu and Fleck (1998) for modelling the scale effect in microindentation of metals.

In this paper we will use a unified theory called gradient elastoplasticity, which is developed in order to overcome complications in the numerical implementation of gradient plasticity. Gradient terms of the strain are introduced in the evolution equations for state variables. As long as the deformation is relatively homogeneous, like in the elastic and hardening regime, these higher order terms are negligible. In the softening regime, however, where deformation becomes strongly inhomogeneous, the gradient terms dominate and the well-posedness of the governing equations is preserved. Gradient elastoplasticity eliminates the need that exists in gradient plasticity to discretise internal variables, like the plastic multiplier and plastic strains, and to apply boundary conditions on them at the elastoplastic boundary. Only the displacement field needs to be discretised, therefore the usual displacement formulation of the finite element method is preserved. Because of the presence of gradient terms in the weak form of the boundary value problem, strains must be continuous so C^1 finite element interpolation is needed.

In the following, we present in Section 2 the theory of gradient elastoplasticity and the expressions for the state variables. The finite element formulation based on C^1 elements is briefly described. In Section 3 we describe the geometry of the model used to simulate the thick-walled cylinder test, along with the necessary boundary conditions and the material parameters. In Section 4 we present numerical results, demonstrating computational robustness in terms of mesh insensitivity and calculated failure mechanisms. The prediction of scale effect is also exhibited, by comparing results from cylinders of different hole size. Final conclusions are drawn in Section 5.

2. Gradient elastoplasticity

In the following we present briefly the theory of gradient elastoplasticity and the basis of its numerical implementation. More detailed derivations and description of the algorithms can be found in Zervos et al. (2001).

2.1. Governing equations

We consider the total strain rate $\dot{\epsilon}_{ij}$ to consist of an elastic part $\dot{\epsilon}^{\mathrm{e}}_{ij}$ and a plastic part $\dot{\epsilon}^{\mathrm{p}}_{ij}$

$$\dot{\epsilon}_{ij} = \dot{\epsilon}^{\mathrm{e}}_{ij} + \dot{\epsilon}^{\mathrm{p}}_{ij} \tag{1}$$

The total (equilibrium) stress rate $\dot{\sigma}_{ij}$ is defined in terms of the elastic strain rate and its Laplacian, as

$$\dot{\sigma}_{ij} = C^{\mathrm{e}}_{ijkl}\left(\dot{\epsilon}^{\mathrm{e}}_{kl} - l^2_{\mathrm{e}}\nabla^2\dot{\epsilon}^{\mathrm{e}}_{kl}\right) \tag{2}$$

where C^{e}_{ijkl} is the tensor of elastic moduli and l_{e} is a material parameter with dimensions of length, called the *elastic material length*.

The yield condition is written

$$F = 0 \tag{3}$$

where $F(\tau_{ij}, \psi)$ is the yield function. The plastic strain rate is defined through a plastic potential $Q(\tau_{ij}, \psi)$ using the flow rule

$$\dot{\epsilon}^{\mathrm{p}}_{ij} = \dot{\psi}\frac{\partial Q}{\partial \tau_{ij}} \tag{4}$$

where the scalar quantity $\dot{\psi}$ is the plastic multiplier. Setting $Q \equiv F$ leads to the special case of associative plasticity.

The yield function F and the plastic potential Q are assumed to depend on the reduced stresses τ_{ij} and on a hardening/softening parameter ψ. The reduced stress rate is given by

$$\dot{\tau}_{ij} = \dot{\sigma}_{ij} - \dot{\alpha}_{ij} \tag{5}$$

and the evolution law for the back stress α_{ij} is

$$\dot{\alpha}_{ij} = -C^{\mathrm{e}}_{ijkl} l^2_{\mathrm{p}} \nabla^2 \dot{\epsilon}^{\mathrm{p}}_{kl} \tag{6}$$

where the scalar parameter l_{p} is called the *plastic material length*. Back stresses develop only where the deformation becomes sufficiently inhomogeneous, allowing for a region around a material point to contribute to its strength.

The plastic multiplier $\dot{\psi}$, and consequently the plastic strains, can be determined from the consistency condition, which ensures that the stress state remains on the yield surface during plastic deformation. This condition is expressed as

$$F(\tau_{ij}, \psi) = 0, \qquad \dot{F}(\tau_{ij}, \psi) = \frac{\partial F}{\partial \tau_{ij}}\dot{\tau}_{ij} + \frac{\partial F}{\partial \psi}\dot{\psi} = 0 \tag{7}$$

Combining Eqs. (1)–(7) and neglecting terms of order higher than second, we arrive at the following equation for the plastic multiplier

$$\begin{aligned}
\left[1 - \frac{H_0}{H}\left(l^2_{\mathrm{e}} + l^2_{\mathrm{p}}\right)\nabla^2\right]\dot{\psi} &= \frac{1}{H}\frac{\partial F}{\partial \tau_{ij}} C^{\mathrm{e}}_{ijkl}\left(\dot{\epsilon}_{kl} - l^2_{\mathrm{e}}\nabla^2\dot{\epsilon}_{kl}\right) \\
H &= H_0 + H_{\mathrm{t}} \\
H_0 &= \frac{\partial F}{\partial \tau_{ij}} C^{\mathrm{e}}_{ijkl}\frac{\partial Q}{\partial \tau_{kl}} \\
H_{\mathrm{t}} &= -\frac{\partial F}{\partial \psi}
\end{aligned} \tag{8}$$

In contrast with classical plasticity, where the consistency condition is an algebraic equation that can be solved analytically, Eq. (8) is a differential equation that would have to be discretised. Nevertheless, this complication can be avoided by solving Eq. (8) analytically in an approximate fashion, as detailed in Zervos et al. (2001). This yields

$$\dot{\psi} = \frac{1}{H}\frac{\partial F}{\partial \tau_{ij}} C^{\mathrm{e}}_{ijkl}\left(\dot{\epsilon}_{kl} + l^2_{\mathrm{c}}\nabla^2\dot{\epsilon}_{kl}\right) \tag{9}$$

with

$$l^2_{\mathrm{c}} = \frac{H_0}{H} l^2_{\mathrm{p}} - \frac{H_{\mathrm{t}}}{H} l^2_{\mathrm{e}} > 0 \tag{10}$$

After some algebraic manipulation, total stress and back stress rates can be expressed in terms of total strain rates as

$$\dot{\sigma}_{ij} = C^{\mathrm{ep}}_{ijkl}\dot{\epsilon}_{kl} - C^{\mathrm{m}}_{ijkl}\nabla^2\dot{\epsilon}_{kl} \tag{11}$$

$$\dot{\alpha}_{ij} = -l^2_{\mathrm{p}} C^{\mathrm{p}}_{ijkl}\nabla^2\dot{\epsilon}_{kl} \tag{12}$$

where C^{p}_{ijkl} is the known *plastic stiffness matrix* of classical plasticity

$$C^{\mathrm{p}}_{ijkl} = \frac{\langle 1 \rangle}{H} C^{\mathrm{e}}_{ijmn} \frac{\partial Q}{\partial \tau_{mn}} \frac{\partial F}{\partial \tau_{st}} C^{\mathrm{e}}_{stkl} \tag{13}$$

and $\langle\ \rangle$ are the McAuley brackets defined by

$$\langle 1 \rangle = \begin{cases} 1, & \text{if } F = 0 \text{ and } \dot{\psi} \geqslant 0 \\ 0, & \text{if } F < 0 \text{ or } F = 0 \text{ and } \dot{\psi} < 0 \end{cases} \tag{14}$$

C^{ep}_{ijkl} is the usual *elastoplastic stiffness matrix*

$$C^{\mathrm{ep}}_{ijkl} = C^{\mathrm{e}}_{ijkl} - C^{\mathrm{p}}_{ijkl} \tag{15}$$

and, finally,

$$C^{\mathrm{m}}_{ijkl} = l^2_{\mathrm{e}} C^{\mathrm{ep}}_{ijkl} + l^2_{\mathrm{c}} C^{\mathrm{p}}_{ijkl} \tag{16}$$

is a stiffness matrix for the second gradient terms.

It is worth noticing that, in the special case of $l_{\mathrm{e}} = 0$ but $l_{\mathrm{p}} \neq 0$, the above equations degenerate to the gradient plasticity model presented by Vardoulakis and Aifantis (1991), Vardoulakis et al. (1992) and Vardoulakis and Frantziskonis (1992). Thus, gradient plasticity is seen as a special case of the theory presented here. Furthermore, for $l_{\mathrm{e}} = l_{\mathrm{p}} = 0$, the classical elastoplasticity theory is recovered.

2.2. Principle of virtual work

As shown by Vardoulakis and Sulem (1995) and Vardoulakis and Aifantis (1991), gradient plasticity can be reinterpreted as a special case of a Mindlin continuum (Mindlin, 1964) in the plastic regime. The idea is readily extended to gradient elastoplasticity, which can be seen as a Mindlin continuum both in the elastic and the plastic regimes (Zervos et al., 2001).

Following the terminology of (Mindlin, 1964) and (Vardoulakis and Aifantis, 1991), we can rewrite Eq. (11) for the total stress rate as

$$\dot{\sigma}_{ij} = \dot{\sigma}^{(0)}_{ij} + \dot{\sigma}^{(2)}_{ij} \tag{17}$$

where

$$\dot{\sigma}^{(0)}_{ij} = C^{\mathrm{ep}}_{ijkl} \dot{\epsilon}_{kl} \tag{18}$$

$$\dot{\sigma}^{(2)}_{ij} = -C^{\mathrm{m}}_{ijkl} \nabla^2 \dot{\epsilon}_{kl} \tag{19}$$

$\dot{\sigma}^{(0)}_{ij}$ is the *Cauchy stress rate*, which is identified as the constitutive stress rate tensor of classical elastoplasticity and it relates to the strain rate. The second term, the *relative stress rate* $\dot{\sigma}^{(2)}_{ij}$, relates to the Laplacian of the strain rate and is equilibrated by a *double stress rate* $\dot{m}_{kij}$, energy conjugate to the strain gradient $\dot{\epsilon}_{ij,k}$. The double stress rate should be such that

$$\dot{\sigma}^{(2)}_{ij} + \dot{m}_{kij,k} = 0 \tag{20}$$

leading to

$$\dot{m}_{kij} = C^{\mathrm{m}}_{ijmn} \dot{\epsilon}_{mn,k} \tag{21}$$

The equations of static equilibrium are obtained through the principle of virtual work. The work of internal forces is written as

$$\delta\dot{W}_{\text{int}} = \int_V \left(\sigma_{ij}^{(0)}\delta\dot{\epsilon}_{ij} + m_{kij}\delta\dot{\epsilon}_{ij,k}\right)\mathrm{d}V \tag{22}$$

To calculate the work of external forces, we split the boundary S in two parts, S_{u} and S_σ. Dirichlet boundary conditions are applied at S_{u}. We remark that, because strain gradients are included in the formulation, the Dirichlet boundary conditions can now contain restrictions not only on the displacement, but on its normal derivative at the boundary as well.

Neumann boundary conditions are applied at S_σ. In the absence of body forces, the external work can be written as an integral over S_σ in the form of

$$\delta\dot{W}_{\text{ext}} = \int_{S_\sigma} \left(t_i\delta\dot{v}_i + \mu_i n_k \delta\dot{v}_{i,k}\right)\mathrm{d}S \tag{23}$$

where t_i is the applied traction vector, μ_i is the applied double traction vector, n_i is the unit normal to S_σ and $\delta\dot{v}_i$ is the virtual displacement rate vector on S_σ. The principle of virtual work can then be written as

$$\int_V \left(\sigma_{ij}^{(0)}\delta\dot{\epsilon}_{ij} + m_{kij}\delta\dot{\epsilon}_{ij,k}\right)\mathrm{d}V = \int_{S_\sigma} \left(t_i\delta\dot{v}_i + \mu_i n_k \delta\dot{v}_{i,k}\right)\mathrm{d}S \tag{24}$$

2.3. Finite Element Formulation

It was shown above that the rates of all constitutive quantities can be expressed in terms of the total strain rate, its gradient and its Laplacian. Therefore, the usual displacement formulation of the finite element method is quite suitable for solving boundary value problems of gradient elastoplasticity. Only the displacement field needs to be discretised, while strains and strain gradients can be computed through shape function derivatives of various orders.

Nevertheless, the presence of strain gradients in the equations of variational equilibrium imposes the extra constraint on strains to be continuous. Since strains are the first derivatives of the displacements, the employed interpolation scheme needs to guarantee C^1 continuity (continuous displacement derivatives), instead of C^0 (continuous displacements) that is sufficient for classical elastoplasticity. In addition, since the strain Laplacian is needed, the shape functions must be polynomials of sufficiently high order, so that they do not vanish when differentiated three times.

The extra continuity needed for the displacement field restricts the choice of elements. In all other aspects, however, the algorithmic procedure to be followed does not differ much from the one used for classical elastoplasticity.

For simplicity, in the following we constrain the analysis to the two-dimensional case of plane strain. We use the three-noded C^1 triangle with 18 degrees of freedom for each interpolated field, shown in Fig. 1. This element is a constrained version of the six-noded C^1 triangle originally presented by Argyris et al. (1968). The displacement field varies as a complete quintic inside the element, while its normal derivative along the element edges is constrained to be cubic. Since the first and second derivatives at the corners suffice to define uniquely a cubic polynomial along each edge, derivatives are continuous across elements. The strain Laplacians vary quadratically. The total degrees of freedom of the element are $2(3 \cdot 6) = 36$, and its shape functions were derived in analytical form by Dasgupta and Sengupta (1990).

The displacement field $\mathbf{u}$ inside each element is interpolated as

$$\mathbf{u} = \begin{Bmatrix} u \\ v \end{Bmatrix} = \mathbf{N} \cdot \hat{\mathbf{u}} \tag{25}$$

where $\mathbf{N}$ is the matrix of the shape functions

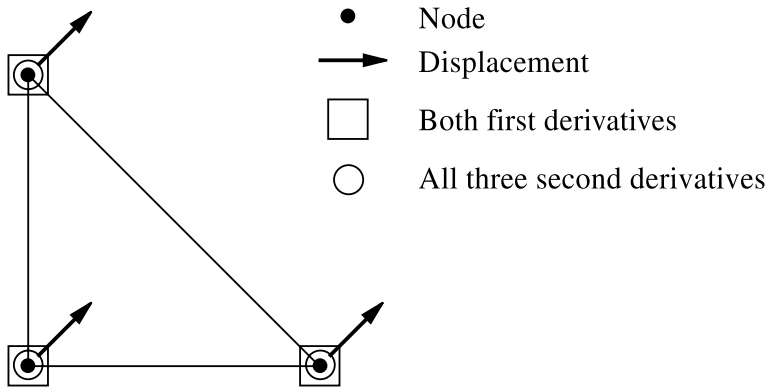

Fig. 1. C^1 triangle with 3 nodes.

$$\mathbf{N} = \left[\begin{array}{c|c|c|c|c|c} N_1 \dots N_6 & 0 \dots 0 & N_7 \dots N_{12} & 0 \dots 0 & N_{13} \dots N_{18} & 0 \dots 0 \\ 0 \dots 0 & N_1 \dots N_6 & 0 \dots 0 & N_7 \dots N_{12} & 0 \dots 0 & N_{13} \dots N_{18} \end{array}\right] \tag{26}$$

and $\hat{\mathbf{u}}$ is the vector of the nodal degrees of freedom

$$\hat{\mathbf{u}} = [\, u_1 \quad u_{1,x} \quad u_{1,y} \quad u_{1,xx} \quad u_{1,xy} \quad u_{1,yy} \quad v_1 \quad \dots \quad v_{1,yy} \quad u_2 \quad \dots \quad v_{2,yy} \quad u_3 \quad \dots \quad v_{3,yy} \,]^{\mathrm{T}} \tag{27}$$

where u is the displacement along the global x-axis, v along the global y-axis and subscripts 1 to 3 refer to the node number. A comma followed by a combination of x and y in the subscript denotes differentiation along each direction mentioned (for example $u_{3,xy}$ is the second order mixed derivative of the displacement along the x-axis on node 3).

Strain rates, their gradients and Laplacians can be written in vector form as

$$\dot{\boldsymbol{\epsilon}} = \mathbf{L}_1 \cdot \mathbf{N} \cdot \hat{\mathbf{u}} = \mathbf{B}_1 \cdot \hat{\mathbf{u}} \tag{28}$$

$$\dot{\boldsymbol{\epsilon}}_x = \frac{\partial}{\partial x}\dot{\boldsymbol{\epsilon}} = \mathbf{L}_{2x} \cdot \mathbf{N} \cdot \hat{\mathbf{u}} = \mathbf{B}_{2x} \cdot \hat{\mathbf{u}} \tag{29}$$

$$\dot{\boldsymbol{\epsilon}}_y = \frac{\partial}{\partial y}\dot{\boldsymbol{\epsilon}} = \mathbf{L}_{2y} \cdot \mathbf{N} \cdot \hat{\mathbf{u}} = \mathbf{B}_{2y} \cdot \hat{\mathbf{u}} \tag{30}$$

$$\nabla^2\dot{\boldsymbol{\epsilon}} = \nabla^2\dot{\boldsymbol{\epsilon}} = \mathbf{L}_3 \cdot \mathbf{N} \cdot \hat{\mathbf{u}} = \mathbf{B}_3 \cdot \hat{\mathbf{u}} \tag{31}$$

where $\mathbf{L}_1$, $\mathbf{L}_{2x}$, $\mathbf{L}_{2y}$ and $\mathbf{L}_3$ are appropriate differential operators. The constitutive relations for the Cauchy stress, double stress and back stress, as expressed in Eqs. (18), (21) and (12) respectively, can then be written in vector form as:

$$\dot{\boldsymbol{\sigma}}^{(0)} = \mathbf{C}^{\mathrm{ep}} \cdot \dot{\boldsymbol{\epsilon}} \tag{32}$$

$$\dot{\mathbf{m}}_x = \mathbf{C}^{\mathrm{m}} \cdot \dot{\boldsymbol{\epsilon}}_x \tag{33}$$

$$\dot{\mathbf{m}}_y = \mathbf{C}^{\mathrm{m}} \cdot \dot{\boldsymbol{\epsilon}}_y \tag{34}$$

$$\dot{\boldsymbol{\alpha}} = -l_{\mathrm{p}}^2 \cdot \mathbf{C}^{\mathrm{p}} \cdot \nabla^2\dot{\boldsymbol{\epsilon}} \tag{35}$$

where $\mathbf{C}^{\mathrm{ep}}$, $\mathbf{C}^{\mathrm{m}}$ and $\mathbf{C}^{\mathrm{p}}$ are the tensors C^{ep}_{ijkl}, C^{m}_{ijkl} and C^{p}_{ijkl} in matrix form.

Substituting the above expressions in the virtual work Eq. (24) we arrive at the following system of equations for the nodal degrees of freedom:

$$\int_V \left(\mathbf{B}_1^{\mathrm{T}}\mathbf{C}^{\mathrm{ep}}\mathbf{B}_1 + \mathbf{B}_{2x}^{\mathrm{T}}\mathbf{C}^{\mathrm{m}}\mathbf{B}_{2x} + \mathbf{B}_{2y}^{\mathrm{T}}\mathbf{C}^{\mathrm{m}}\mathbf{B}_{2y}\right)\mathrm{d}V \cdot \hat{\mathbf{u}} = \int_{S_\sigma} \left[\mathbf{N}^{\mathrm{T}}\hat{\mathbf{t}} + \left(n_x\frac{\partial \mathbf{N}^{\mathrm{T}}}{\partial x} + n_y\frac{\partial \mathbf{N}^{\mathrm{T}}}{\partial y}\right)\hat{\mathbf{m}}\right]\mathrm{d}S \tag{36}$$

where $\hat{\mathbf{t}}$ is the boundary traction vector, $\hat{\mathbf{m}}$ is the boundary double traction vector and $\mathbf{n} = [n_x, n_y]$ is the outward unit normal to the boundary.

The integral on the left hand side expresses the *stiffness matrix*. The right hand side integral is the *load vector*. In classical plasticity only the first term of both integrands is present. The discretised gradient plasticity model is thus obtained by extending the finite element formulation of classical elastoplasticity to include additional entries in the stiffness matrix and loading vector.

Eq. (36) is solved iteratively with the Newton–Raphson method. At the end of each iteration, the current estimate of the solution vector $\hat{\mathbf{u}}$ is used to calculate the Cauchy stresses and the double stresses, which are in turn used to calculate the residual forces at the end of the iteration as

$$\mathbf{R} = \int_V \left(\mathbf{B}_1^{\mathrm{T}}\boldsymbol{\sigma}^{(0)} + \mathbf{B}_{2x}^{\mathrm{T}}\mathbf{m}_x + \mathbf{B}_{2y}^{\mathrm{T}}\mathbf{m}_y\right)\mathrm{d}V - \int_{S_\sigma} \left[\mathbf{N}^{\mathrm{T}}\hat{\mathbf{t}} + \left(n_x\frac{\partial \mathbf{N}^{\mathrm{T}}}{\partial x} + n_y\frac{\partial \mathbf{N}^{\mathrm{T}}}{\partial y}\right)\hat{\mathbf{m}}\right]\mathrm{d}S \tag{37}$$

3. Model description

3.1. Geometry, loading and boundary conditions

In the following we present results of numerical simulations of thick-walled cylinder tests, which are the standard tests used in the petroleum industry for modelling the mechanical behaviour of boreholes and perforations. Because of the scale effect clearly observed in the experiment, proper interpretation of the experimental data and correct extrapolation to field predictions are challenging issues. We repeat that classical elastoplasticity is unable to predict the experimentally observed scale effect since it does not include a material length for scaling the size of the holes.

The geometry of the problem and the loading and boundary conditions are shown in Fig. 2. Assuming symmetry along the x- and y-axes, only one quarter of the specimen needs to be discretised. The ratio of the

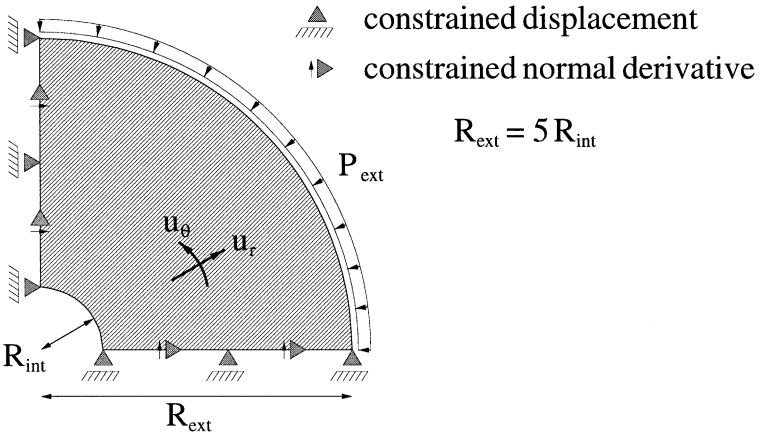

Fig. 2. Model geometry, loading and boundary conditions.

external to the internal radius is 5:1. The cylinder is loaded with increasing uniform pressure on the external boundary while the internal pressure is maintained to zero.

Special attention must be given to the kinematic boundary conditions needed to establish the two symmetry boundaries along the x- and y-axes. As we mentioned earlier, the existence of gradient terms in the equations of variational equilibrium allows, in addition to the displacement, for its normal to the boundary derivative to be prescribed as well. Therefore, in order to establish symmetry boundary conditions along the x- and y-axes not only displacements but higher order constraints are also needed to be prescribed.

Examining intuitively the behaviour of the radial and tangential displacements u_r and u_θ on both sides of the symmetry boundaries, we remark the following: u_θ must be antisymmetric (for example, for the x-axis, $u_\theta(-\theta) = -u_\theta(\theta)$), hence $u_\theta(0) = u_\theta(\pi/2) = 0$. This is the first kinematic constraint to be applied. It is equivalent to prescribing $u_x = 0$ along the y-axis and $u_y = 0$ along the x-axis. The antisymmetry condition for u_θ means that, although we can determine its value at the symmetry boundary, its normal derivative remains unknown and can even vary along the boundary. On the other hand, u_r must be symmetric around the symmetry boundaries (for example, for the x-axis, $u_r(-\theta) = u_r(\theta)$). Although the value of u_r on the boundary is unknown, the symmetry condition implies that its derivative with respect to θ must be zero, $(\partial u_r/\partial\theta)(0) = (\partial u_r/\partial\theta)(\pi/2) = 0$. This is the second kinematic constraint to be applied. It is equivalent to prescribing $\partial u_y/\partial x = 0$ along the y-axis and $\partial u_x/\partial y = 0$ along the x-axis.

3.2. Material model

The material behaviour is described by the Mohr–Coulomb failure criterion

$$F = m\tau_1 - \tau_3 - \sigma_c = 0 \tag{38}$$

where $m = (1 + \sin\phi)/(1 - \sin\phi)$ is the friction coefficient and $\sigma_c = (2c\cos\phi)/(1 - \sin\phi)$ is the *equivalent stress*; ϕ is the angle of internal friction and c is the material cohesion. The material parameters were calibrated from triaxial tests on Castlegate sandstone. The elastic constants were found to be $E = 8100$ MPa and $v = 0.35$. The friction angle is considered constant, with a value $\phi = 32.54°$ and an associated flow-rule is assumed, $Q = F$.

The hardening/softening behaviour is defined through the equivalent stress $\sigma_c(\epsilon_p)$, which depends on the accumulated *equivalent plastic strain* ϵ_p. The equivalent plastic strain rate is defined as the rate of dissipated work due to plastic deformation, divided by the equivalent stress. The hardening law is taken to evolve according to the hyperbolic equation

$$\sigma_c(\epsilon_p) = \sigma_{c,0} + \frac{(1 - C_0\epsilon_p)\epsilon_p}{C_1 + C_2\epsilon_p} \tag{39}$$

which is fitted on the experimental data. $C_1 = 1.323 \times 10^{-5}$ and $C_2 = 6.1271 \times 10^{-2}$ are calibration constants and $\sigma_{c,0} = 25$ MPa defines the state of initial yield.

The constant C_0 is an open parameter which controls the rate of softening; in this study it is taken to be $C_0 = 70$. The plastic material length is set to $l_p = 0.2$ mm, equal to the mean grain diameter of the Castlegate sandstone. The elastic material length is taken to be 10 times smaller, $l_e = 0.02$ mm. This choice is made more or less arbitrarily in this study, and reflects the fact that the existence of microstructure is more dominant in the plastic regime. We also note that, due to diffuse and localised bifurcations and end restraints, standard laboratory calibration tests cannot determine the "true" material softening. In principle, extra information on the shear band thickness and the scale effect could be inverted using the gradient elastoplasticity model to obtain the softening rate and the material lengths.

4. Numerical results and discussion

4.1. Mesh sensitivity study

In order to demonstrate mesh insensitivity of the results, computations were carried out for three different meshes (coarse, medium and fine) presented in Table 1. A picture of the mesh near the hole is shown in Fig. 3(a), for the case of the medium mesh. The model presented in the following has internal radius $r_i = 0.10$ m and external $r_e = 0.50$ m.

Upon loading, the stress concentration near the hole wall causes the material there to yield first. The material follows the hardening branch and then enters the softening regime as plastic deformation con-

Table 1
Finite element meshes

Name	Nodes	Elements	Degrees of freedom
Coarse	$15 \times 41 = 615$	1120	7380
Medium	$20 \times 81 = 1620$	3040	19 440
Fine	$25 \times 121 = 3025$	5760	36 300

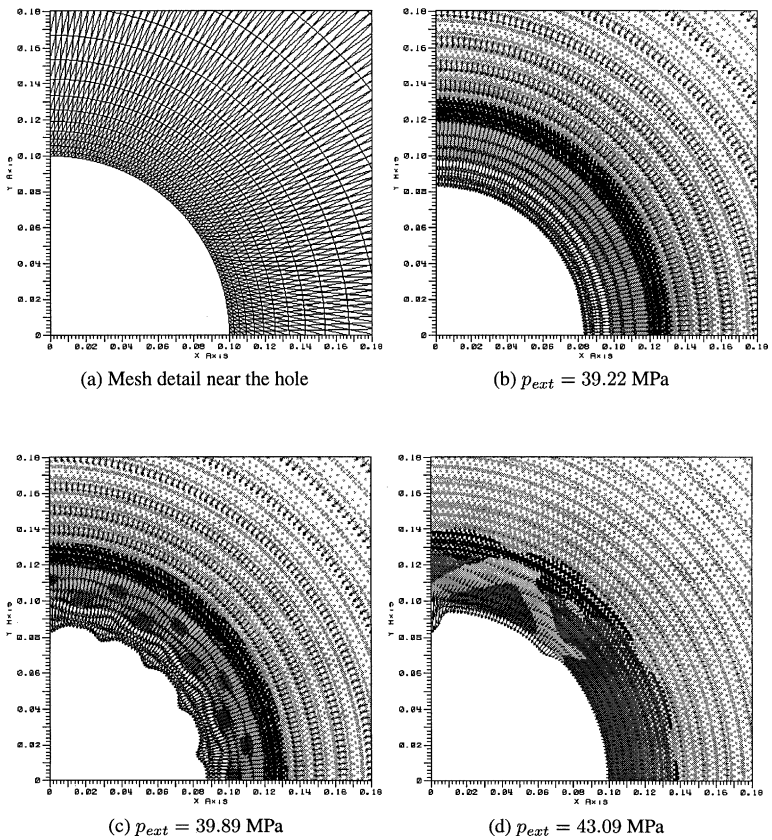

(a) Mesh detail near the hole (b) $p_{ext} = 39.22$ MPa

(c) $p_{ext} = 39.89$ MPa (d) $p_{ext} = 43.09$ MPa

Fig. 3. (a) Mesh, (b)–(d) progressive localisation shown by the incremental displacement field and material state for medium mesh ($r_i = 0.10$ m).

tinues. Because of the imposed symmetries on geometry and loading, the deformation is initially axisymmetric. This can be seen by the vector plot of Fig. 3(b), which shows convergence of the hole in terms of the displacement increment. In the same plot we can see that a zone of softening material forms around the hole wall (light grey points), surrounded by a zone of hardening material (black points). The rest of the material in the deeper region is still virgin elastic, since stresses there are not beyond initial yield.

Upon further loading, however, the axisymmetry of the deformation breaks spontaneously. As it can be seen in Fig. 3(c), the displacement increment takes a sinusoidal form. As a result, regions of the material which were in the plastic regime now unload elastically (dark grey points). As the load increases the unloading "spots" grow in size and coalesce. Finally, almost all the region close to the hole wall is unloading elastically, except the narrow zones of the forming shear-bands, which continue to plastically soften (Fig. 3(d)). The bands are connected to a familiar breakout form, which resembles the failure mechanisms observed in the experiments.

It should be noted that, although axisymmetry breaks and unloading takes place, the external load keeps increasing. In other words we observe a "tangential bifurcation". The load eventually reaches a peak and then drops, as the deformation localises. It is also worth noticing that loss of symmetry is totally spontaneous. Neither was the solution biased with a preselected eigenmode, nor were imperfect elements introduced in the model. Imperfect elements are needed in the modelling of homogeneous problems such as the biaxial test (Zervos et al., 2001). In the present problem the deformation is inhomogeneous due to the stress concentration near the hole wall from the early beginning. It seems that the round-off error alone suffices to push the solution to a localised pattern. The same observation was made by Papanastasiou and Vardoulakis (1992), where progressive localisation in thick-walled cylinders was studied with a Cosserat continuum. The imperfection sensitivity of these models means that close to a bifurcation point any "real" imperfection will push the solution away from the primary solution towards the localisation branch.

From the external pressure vs. hole closure curve of Fig. 4, we see that all three meshes predict the same response. The load where axisymmetry breaks is the same for all models, and the same is the pattern with

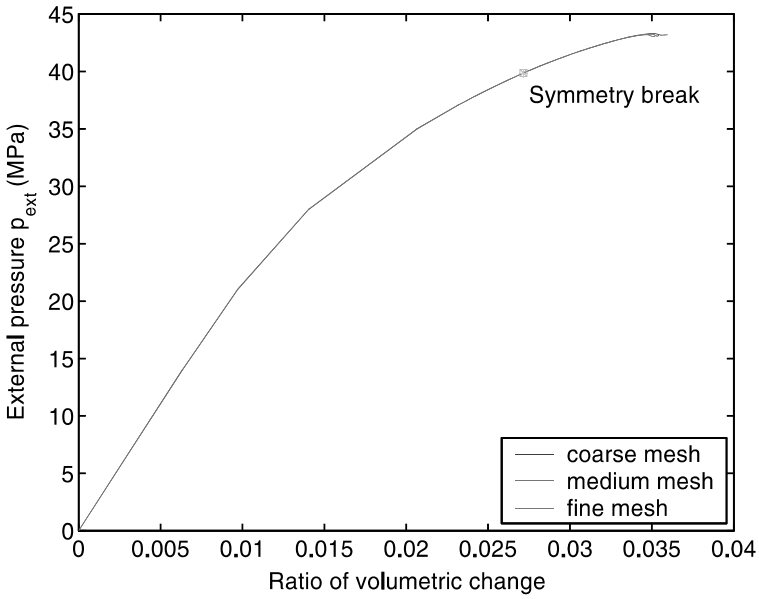

Fig. 4. External pressure vs. hole closure for three different meshes, $r_i = 0.10$ m.

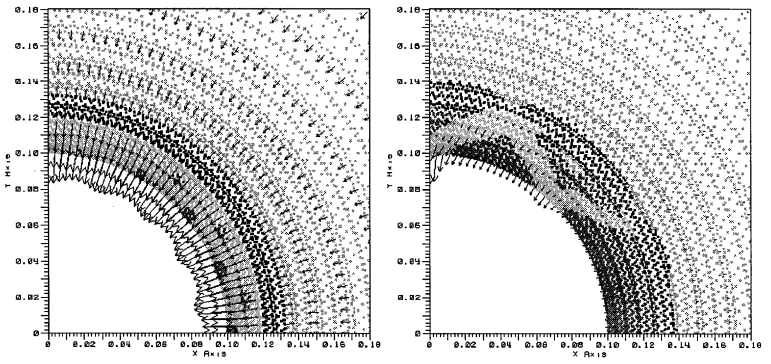

(a) $p_{ext} = 39.87$ MPa (b) $p_{ext} = 43.20$ MPa

Fig. 5. Progressive localisation shown by the incremental displacement field and material state for coarse mesh ($r_i = 0.10$ m).

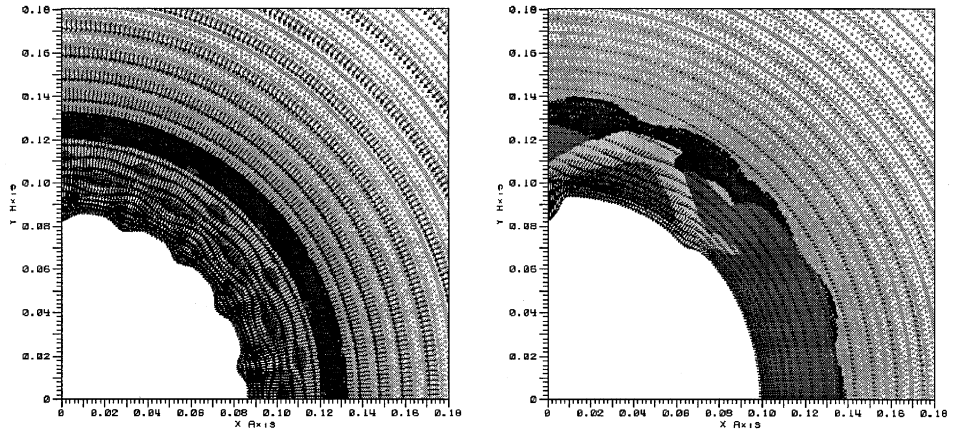

(a) $p_{ext} = 39.87$ MPa (b) $p_{ext} = 43.05$ MPa

Fig. 6. Progressive localisation shown by the incremental displacement field and material state for fine mesh ($r_i = 0.10$ m).

which it breaks (the number of waves of the sinusoidal around the hole, or *warping mode*). This can be seen by comparing Fig. 3(c) with Fig. 5(a) for the coarse mesh, and Fig. 6(a) for the fine mesh. The final localised patterns, shown in Figs. 3(d), 5(b), and 6(b), are the same as well.

4.2. Scale effect

In order to demonstrate the scale effect, computations were carried out for models with different internal radii. Apart from the case of $r_i = 0.10$ m, which was already presented, models with $r_i = 0.02$, 0.05, 0.15, 0.20 and 0.40 m were run. The ratio of the external radius to the internal was kept fixed to 5:1 for all models. The results are briefly presented in Table 2, where p_{symm} is the load at which symmetry breaks and p_{peak} is the peak load. The ratio of the hole radius over the plastic internal length, the type of mesh used and the pattern with which symmetry breaks (warping mode) are also shown.

Table 2
Results for models of various sizes

r_i	r_i/l_p	Mesh	Warping mode (quarter)	p_{symm}	p_{peak}
0.02	100	Coarse	–	–	52.02
0.05	250	Coarse	2	47.57	48.98
	500	Coarse	4.5	39.71	43.32
0.10					
0.10	500	Medium	4.5	39.71	43.25
0.10	500	Fine	4.5	39.71	43.20
	750	Medium	8	37.44	39.92
0.15					
0.20	1000	Medium	10	37.21	38.68
0.40	2000	Medium	21.5	37.06	37.24

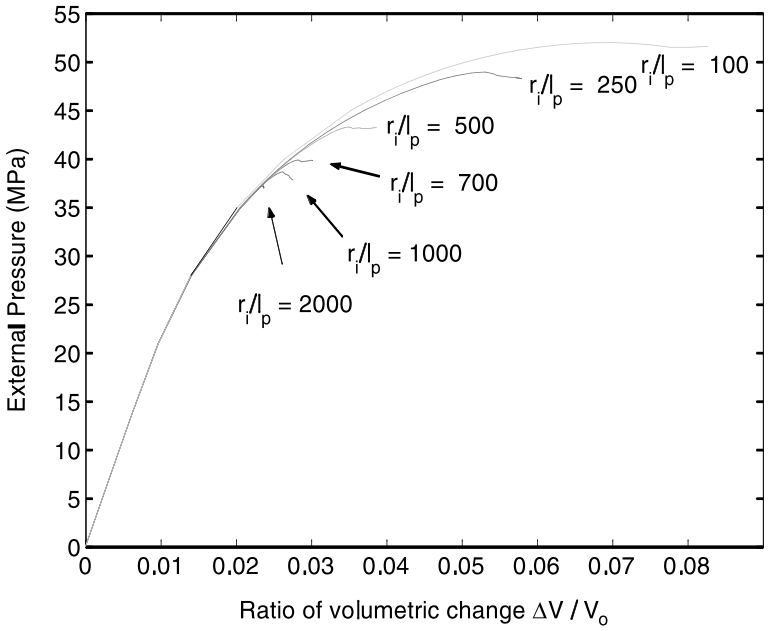

Fig. 7. External pressure vs. hole closure for models with different size holes.

The external pressure vs. hole closure curve for each model is presented in Fig. 7. The various secondary branches which correspond to different hole radii demonstrate that small holes are stronger than large ones. From this figure and Table 2, it is clear that both p_{symm} and p_{peak} increase as the hole radius decreases. For the smallest hole presented, the one with $r_i = 0.02$ m, symmetry never breaks. Also, smaller holes give lower warping modes, which is consistent with Papanastasiou and Vardoulakis (1992). It is worth noticing the behaviour of the model with $r_i = 0.40$ m in particular, where structural softening is very severe showing the curve to drop almost vertically once a critical deformation in the localisation branch is reached.

Another observation we can make is that as the hole gets larger, the scale effect becomes less pronounced. For example, the difference between $r_i = 0.05$ m and $r_i = 0.10$ m is much bigger than the one between $r_i = 0.20$ m and $r_i = 0.40$ m. This is clearly shown in the scale diagram of Fig. 8, where p_{peak} and p_{symm} are plotted vs. r_i/l_p, which is a measure of the hole size. The scale effect fades out rapidly with

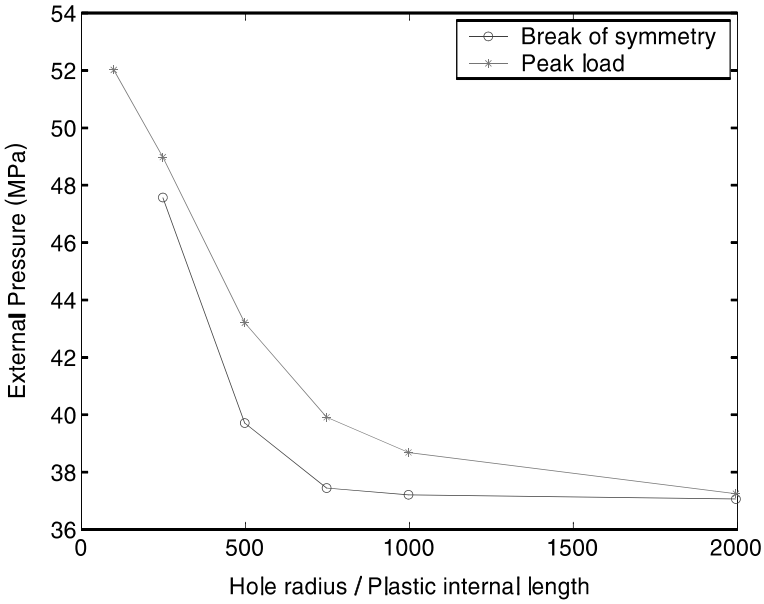

Fig. 8. Dependence of thick-walled cylinder failure load on dimensionless hole size (scale effect).

increasing hole size, a tendency also observed in the experiment (Haimson and Herrick, 1988; Papamichos and van den Hoek, 1995).

5. Conclusions

The theory of gradient elastoplasticity, developed by Zervos et al. (2001) and presented briefly here with its numerical implementation, was used to model the progressive failure and the scale effect observed in thick-walled cylinders. The material is a weak sandstone modelled as a Mohr–Coulomb dilatant material with hardening and softening behaviour. The inclusion of gradient terms regularises the material behaviour in the softening regime. The mesh dependence inherent in classical plasticity is remedied.

The model predicts that symmetry of deformation breaks spontaneously according to a dominant warping mode. This takes place in the branch of structural hardening before the peak load is reached. The deformation localises progressively into thin shear bands while the surrounding material unloads elastically. The localised deformation leads to failure patterns similar to the breakout form observed in experiments. Mesh-insensitivity was demonstrated by showing that the predicted bifurcation mode, the final deformation pattern and the load–displacement curves are the same for different meshes. The model can also predict the existence of the scale effect according to which small holes are much stronger than large holes.

Acknowledgements

The authors would like to thank Schlumberger Cambridge Research for supporting this research. I. Vardoulakis wants also to acknowledge GSRT of Greece for supporting his research through the program PENED 99 ED 642.

References

Aifantis, E., 1984a. On the microstructural origin of certain inelastic models. ASME J. Engng. Mater. Technol. 106, 326–330.

Aifantis, E., 1984b. Remarks on media with microstructures. Int. J. Engng. Sci. 22, 961–968.

Aifantis, E., 1987. The physics of plastic deformation. Int. J. Plasticity 3, 211–247.

Argyris, J.H., Fried, I., Scharpf, D.W., 1968. The TUBA family of plate elements for the matrix displacement method. Aeronaut. J. Roy. Aeronaut. Soc. 72, 701–709.

Dasgupta, S., Sengupta, D., 1990. A higher-order triangular plate bending element revisited. Int. J. Num. Meth. Engng. 30, 419–430.

Fleck, N.A., Hutchinson, J.W., 1993. A phenomenological theory for strain gradient effects in plasticity. J. Mech. Phys. Solids 41 (12), 1825–1857.

Haimson, B., Herrick, C., 1988. Borehole breakouts and in situ stress. In: Rowley, J. (Ed.), Drilling Symposium 1989. pp. 17–22.

Mihashi, M., Okamura, H., Bažant, Z., 1994. Size effect in concrete structures. E&FN Spon.

Mindlin, R., 1964. Microstructure in linear elasticity. Arch. Rat. Mech. Anal. 10, 51–78.

Mühlhaus, H.-B., Vardoulakis, I., 1987. The thickness of shear bands in granular materials. Geotechnique 37, 271–283.

Pamin, J., 1994. Gradient-Dependent Plasticity in Numerical Simulation of Localization Phenomena, PhD Thesis. Delft University Press.

Papamichos, E., van den Hoek P., 1995. Size dependency of Castlegate and Berea sandstone hollow-cylinder strength on the basis of bifurcation theory. Proc. 35th US Symp. Rock Mechanics.

Papanastasiou, P., Durban, D., 1999. Bifurcation of elastoplastic pressure-sensitive hollow cylinders. J. Appl. Mech. 66, 117–123.

Papanastasiou, P., Vardoulakis, I., 1989. Bifurcation analysis of deep boreholes: II. Scale effect. Int. J. Num. Anal. Meth. Geomech. 13, 183–198.

Papanastasiou, P., Vardoulakis, I., 1992. Numerical treatment of progressive localization in relation to borehole stability. Int. J. Num. Anal. Meth. Geomech. 16, 389–424.

Pijaudier-Cabot, G., Bažant, Z., 1987. Nonlocal damage theory. J. Engng. Mech. ASCE 113, 1512–1533.

Ramaswamy, S., Aravas, N., 1998a. Finite element implementation of gradient plasticity models. part I: Gradient-dependent yield functions. Comput. Meth. Appl. Mech. Engng. 163, 11–32.

Ramaswamy, S., Aravas, N., 1998b. Finite element implementation of gradient plasticity models. part II: Gradient-dependent evolution equations. Comput. Meth. Appl. Mech. Engng. 163, 33–53.

Shu, J.Y., Fleck, N.A., 1998. The prediction of a size effect in microindentation. Int. J. Solids Struct. 35 (13), 1363–1383.

Tvergaard, V., Needleman, A., 1995. Effects of nonlocal damage in porous plastic solids. Int. J. Solids Struct. 32, 1063–1077.

van Vliet, M., 2000. Size effect in tensile fracture of concrete and rock, PhD Thesis. Delft University Press.

Vardoulakis, I., Aifantis E.C, 1991. A gradient flow theory of plasticity for granular materials. Acta Mech. 87, 197–217.

Vardoulakis, I., Frantziskonis, G., 1992. Micro-structure in kinematic-hardening plasticity. Eur. J. Mech. A /Solids 11 (4), 467–486.

Vardoulakis, I., Papamichos, E., Sulem, J., 1994. A second-gradient plasticity model for granular rocks. In: Bažant, M.J.Z.P., Bittnar, Z., Jirásek, M., Mazars, J. (Eds.), Fracture and Damage in Quasibrittle Structures. E&FN Spon.

Vardoulakis, I., Papanastasiou, P., 1988. Bifurcation analysis of deep boreholes: I. surface instabilities. Int. J. Num. Anal. Meth. Geomech. 12, 379–399.

Vardoulakis, I., Shah, K.R., Papanastasiou, P., 1992. Modelling of tool-rock shear interfaces using gradient-dependent flow theory of plasticity. Int. J. Rock Mech. Min. Sci. & Geomech. Abstr. 29 (6), 573–582.

Vardoulakis, I., Sulem, J., 1995. Bifurcation Analysis in Geomechanics. Blackie Academic and Professional.

Zervos, A., Papanastasiou, P., Vardoulakis, I., 2001. A finite element displacement formulation for gradient elastoplasticity. Int. J. Num. Meth. Engng., in press.